Chapter 2

Study of Excitation functions of heavy residues produced in the reaction of ^{14}N+^{103}Rh

Contents

⋆ The work presented in this chapter has been published in a Peer-Reviewed Journal (J. Acharya, S. Mukherjee, *et al.*, Phys. Rev. C **93**, 024608 (2016)) and the license/permission has been obtained by the author from the journal to reuse the published work here as a part of this thesis (License Number: RNP/21/MAY/039589).

The excitation functions of heavy residues, produced in the interaction of ^{14}N with ^{103}Rh, have been measured over the projectile energy region from a threshold up to 400 MeV by means of the activation method in conjunction with γ-ray spectroscopy. Cross sections for 15 reaction residues are presented, namely, ^{104}Cd, $^{103-105}Ag$, $^{99-101}Pd$, $^{97,99,101}Rh$, $^{95,97}Ru$ and $^{94-96}Tc$. The experimental data are compared with theoretical model predictions using the hybrid Monte Carlo simulation model as implemented in the recently released ALICE2014 code. The theory assumes that the dominant pre-equilibrium mechanism includes multinucleon and cluster emissions in the initial stages of the interaction between the projectile and the target nucleus. Overall, the theoretical predictions provide a satisfactory agreement with the trend of the present experimental results for most of the observed reaction residues. This provides strong evidence that the underlying reaction mechanisms in the code are appropriately described. Overall, the Obninsk level densities give the best results in the present study.

2.1 Introduction

In heavy-ion reactions, a complex series of processes can occur due to the relatively large number of nucleons involved as well as a large amount of angular momenta that a projectile can transfer to the target nucleus. These processes include the formation of an excited intermediate nucleus in a state far from statistical equilibrium, its equilibration by means of intranuclear interactions, pre-equilibrium emission of nucleons and light clusters, and finally the formation of an intermediate equilibrated nucleus, which further evaporates particles and emits γ -rays and/or fission [1–4]. There is a statistical competition between these different reaction mechanisms, which all contribute to the cross sections for the formation of specific heavy residues. It has been known for many years that the small but measurable cross sections for the formation of some of the heavy residues cannot be accounted for by considering only evaporation of particles from an equilibrated compound nucleus. Even at incident energies barely higher than the Coulomb barrier, pre-equilibrium emission of nucleons during the thermalization of the composite nucleus has to be taken into consideration in order to reproduce the formation cross sections of the heavy (target-like) residues [5].

In recent years, a significant body of experimental data on excitation functions, forward recoil ranges, and angular distributions of residues has been accumulated at incident energies up to 400 MeV [2,3,6–8] in the mass region similar to the present work. This allowed a comprehensive analysis of all the processes which take place, both in the initial projectile-target interaction and during the deexcitation of the nonequilibrated hot nuclei which are produced in the interaction. The analysis of these data have suggested that, in addition to the contributions from projectile fragmentation, deep inelastic collisions, or other non-fusion processes, a significant amount of pre-equilibrium particles are also emitted. The possible importance of pre-equilibrium decay in heavy-ion reactions has been discussed earlier by Blann [9] and Blann and Vonach [10]. Furthermore, a large fraction of alpha particles which initially participated in the incomplete fusion processes is emitted in the pre-equilibrium stage as well.

The yields of residues formed by α -particle emission should differ appreciably for the respective contributing reaction mechanisms, which depend sensitively on the incident projectile energy. There exists experimental evidence of a pre-equilibrium nucleon and alpha particle emission that contribute significantly to the subsequent deexcitation following the fusion of heavy ions [11,12]. In nuclear reactions at intermediate energies, a wide variety of residues is produced. The yields, energy spectra, and angular distributions are valuable information for applications and interdisciplinary fields [13]. The development of phenomenological theories is important in the physics of such reaction data. Earlier, basic reaction models, such as the exciton model [14] and the geometry-dependent hybrid model [11,15], were being employed for analyzing these data, in particular, for their description of pre-equilibrium reactions. However, a comparison of measurements with the model predictions often showed limited success, especially for reactions induced by heavy ions.

Cavinato *et. al.* [1] and Buthelezi *et. al.* [2,3] presented excitation function data as well as energy spectra and angular distributions of alpha particles and intermediate mass fragments (IMFs) for ^{12}C+^{103}Rh and ^{16}O+^{103}Rh systems from the Coulomb barrier up to 400 MeV. In order to understand these data, complete fusion and break-up-fusion processes were assumed to depend on the mean-field interaction between the target and the projectile nuclei. The evolution of the system towards equilibrium was studied by following the nucleon-nucleon cascade solving a set of Boltzmann master equations. The model was successful in arriving at a generally good agreement between the measured data and the theoretical predictions.

Recently, a new version of the code ALICE [11–13,16–18], namely, ALICE2014, has become available, providing a theoretical framework for calculating cross sections for the production of residues at intermediate energies. The new code incorporates the Hybrid Monte Carlo simulation (HMS) model for calculating cross sections for pre-equilibrium reactions induced by light and heavy ions. It includes multiple pre-equilibrium emission processes as well as a semiclassical treatment of angular momentum transfer effects. Considering the wide use of the HMS model in applications and to ensure its predictive power, it is important to expose the code to a wide variety of reactions, especially for reactions induced by different medium-mass and heavy ions.

In this work, excitation functions for the formation of residues in the interaction of ^{14}N projectiles with ^{103}Rh target nuclei were measured from the Coulomb barrier up to 400 MeV. The experiment presented here was designed to establish the extent to which pre-equilibrium emission of alpha particles is present in heavy-ion reactions leading to the heavy fusionlike and targetlike residues. The use of ^{14}N projectiles enhances the data set for comparisons as data for ^{12}C and ^{16}O induced reactions have already been measured on this nucleus [1–3]. It provides a valuable testing ground for the HMS model. In particular, it may be interesting to look for differences in the α -particle and IMF emission spectra as well as the heavy residues left behind from the interactions of a projectile that is not a pure alpha-like nucleus, such as ^{12}C and ^{16}O. Here we present the excitation functions for heavy reaction residues, and a separate investigation on the emission spectra of light clusters is presented in next chapter. Also, the present experimental data, is a useful addition to the global nuclear database in this mass region.

2.2 Experimental Details

In the present investigation, excitation functions for 15 reaction residues were measured, namely, ^{104}Cd, $^{103-105}Ag$, $^{99-101}Pd$, $^{97,99,101}Rh$, $^{95,97}Ru$, and $^{94-96}Tc$ for the system of ^{14}N+^{103}Rh up to 400 MeV using the activation technique in conjunction with off-line γ -ray spectroscopy. The separated sector cyclotron (SSC) of iThemba LABS, capable of accelerating ^{14}N ions up to several tens of MeV nucleon, provided the ^{14}N beam with an incident energy of 250 MeV and 400 MeV. The beam formation started with an external cyclotron resonance ion source, followed by injection into a solid pole cyclotron SPC2 which is an injector cyclotron for further acceleration. The SSC provided the final acceleration for the desired beam energy.

The beam current intercepted by the target and beam stop was measured with a Brookhaven Instruments model 1000C current integrator. The accumulated charge was also logged in at 10 second intervals by means of the data-acquisition system XSYS. In this way the beam intensity fluctuations during bombardments were monitored. This was performed because beam fluctuations may yield inaccuracies in the results, especially in the case of radionuclides with half-lives shorter than or on the same order of magnitude as the bombardment time if not properly corrected for.

A metallic Rh foil stack was prepared for bombardment with a ^{14}N beam. Self-supporting foils of 99.99% purity were supplied by Goodfellow Ltd. (Cambridge, U.K.). The stack consisted of a single 5-μm-thick Ti monitor foil, followed by several Rh foils with nominal thicknesses of 310 $\mu g/cm^2$. These Rh foils were backed with 0.0015 mm thick Mylar, interspaced with 2.92 mg/cm^2 aluminium catchers and 6.75 mg/cm^2 aluminium degraders. In the first irradiation, the energy of 250 MeV beam decreased through the stack from 250 MeV to 89.4 MeV in energy steps varying from 10 to 20 MeV. In the second irradiation, the energy of 400 MeV beam decreased through the stack from 400 MeV to 240.2 MeV in energy steps varying from 7 to 10 MeV. Table 2.1 and Table 2.2 shows the stack foil arrangement and energy degradation in each target foil at 250 and 400 MeV respectively. The thickness of the stack was such that it stopped the beam. It was irradiated for 2 hrs. at an incident energy of 250 MeV and 400 MeV and an average beam current of 20 nA. Afterwards, an autoradiogram of the Ti foil confirmed that the focus of the beam remained on the center of the stack for the entire duration of

Table 2.1: Energy degradation at each foil for incident beam energy of 250 MeV

FOIL NO.	THICKNESS (g/cm^2)	E (IN) (MeV)	E (OUT) (MeV)	E (LOST) (MeV)	FOIL TYPE
1	0.00031	250	249.756	0.244	Rh
2	0.00021	249.756	249.484	0.272	Mylar
3	0.00292	249.484	246.371	3.113	Al-cat
4	0.00675	246.371	239.044	7.327	Al-deg
5	0.00031	239.044	238.791	0.253	Rh
6	0.00021	238.791	238.509	0.282	Mylar
7	0.00292	238.509	235.284	3.226	Al-cat
8	0.00675	235.284	227.68	7.604	Al-deg
9	0.00031	227.68	227.418	0.262	Rh
10	0.00021	227.418	227.125	0.293	Mylar
11	0.00292	227.125	223.771	3.353	Al-cat
12	0.00675	223.771	215.854	7.917	Al-deg
13	0.00031	215.854	215.582	0.272	Rh
14	0.00021	215.582	215.276	0.306	Mylar
15	0.00292	215.276	211.778	3.498	Al-cat
16	0.00675	211.778	203.501	8.276	Al-deg
17	0.00031	203.501	203.217	0.285	Rh
18	0.00021	203.217	202.896	0.321	Mylar
19	0.00292	202.896	199.23	3.666	Al-cat
20	0.00675	199.23	190.537	8.693	Al-deg
21	0.00031	190.537	190.238	0.299	Rh
22	0.00021	190.238	189.9	0.338	Mylar
23	0.00292	189.9	186.038	3.862	Al-cat
24	0.00675	186.038	176.852	9.186	Al-deg
25	0.00031	176.852	176.537	0.315	Rh
26	0.00021	176.537	176.178	0.359	Mylar
27	0.00292	176.178	172.082	4.096	Al-cat
28	0.00675	172.082	162.301	9.781	Al-deg
29	0.00031	162.301	161.966	0.335	Rh
30	0.00021	161.966	161.581	0.384	Mylar
31	0.00292	161.581	157.199	4.382	Al-cat
32	0.00675	157.199	146.681	10.519	Al-deg
33	0.00031	146.681	146.32	0.36	Rh
34	0.00021	146.32	145.904	0.416	Mylar
35	0.00292	145.904	141.161	4.743	Al-cat
36	0.00675	141.161	129.694	11.467	Al-deg
37	0.00031	129.694	129.302	0.392	Rh

Table 2.1 continued from previous page

38	0.00021	129.302	128.844	0.458	Mylar
39	0.00292	128.844	123.626	5.218	Al-cat
40	0.00675	123.626	110.876	12.75	Al-deg
41	0.00031	110.876	110.44	0.436	Rh
42	0.00021	110.44	109.923	0.516	Mylar
43	0.00292	109.923	104.04	5.884	Al-cat
44	0.00675	104.04	89.415	14.624	Al-deg
45	0.00031	89.415	88.914	0.501	Rh
46	0.00021	88.914	88.309	0.606	Mylar
47	0.00292	88.309	81.396	6.913	Al-cat
48	0.00675	81.396	63.637	17.759	Al-deg
49	0.00031	63.637	63.025	0.612	Rh
50	0.00021	63.025	62.256	0.769	Mylar
51	0.00292	62.256	53.417	8.839	Al-cat
52	0.00675	53.417	28.5	24.916	Al-deg
53	0.00031	28.5	27.626	0.874	Rh
54	0.00021	27.626	26.374	1.251	Mylar
55	0.00292	26.374	11.286	15.088	Al-cat

the bombardment. The beam energy was determined by means of a calibrated 90°analysis magnet with an uncertainty of less than 1 MeV.

Table 2.2: Energy degradation at each foil for incident beam energy of 400 MeV

FOIL NO.	THICKNESS (g/cm^2)	E (IN) (MeV)	E (OUT) (MeV)	E (LOST) (MeV)	FOIL TYPE
1	0.00031	400	399.829	0.171	Rh
2	0.00021	399.829	399.643	0.186	Mylar
3	0.00292	399.643	397.502	2.14	Al-cat
4	0.00675	397.502	392.513	4.99	Al-deg
5	0.00031	392.513	392.339	0.174	Rh
6	0.00021	392.339	392.15	0.189	Mylar
7	0.00292	392.15	389.977	2.173	Al-cat
8	0.00675	389.977	384.911	5.067	Al-deg
9	0.00031	384.911	384.734	0.177	Rh
10	0.00021	384.734	384.542	0.192	Mylar
11	0.00292	384.542	382.336	2.207	Al-cat
12	0.00675	382.336	377.188	5.148	Al-deg
13	0.00031	377.188	377.009	0.179	Rh
14	0.00021	377.009	376.814	0.195	Mylar
15	0.00292	376.814	374.571	2.243	Al-cat
16	0.00675	374.571	369.338	5.233	Al-deg
17	0.00031	369.338	369.156	0.182	Rh
18	0.00021	369.156	368.958	0.198	Mylar
19	0.00292	368.958	366.677	2.281	Al-cat
20	0.00675	366.677	361.354	5.323	Al-deg
21	0.00031	361.354	361.169	0.185	Rh
22	0.00021	361.169	360.967	0.202	Mylar
23	0.00292	360.967	358.646	2.321	Al-cat
24	0.00675	358.646	353.228	5.418	Al-deg
25	0.00031	353.228	353.039	0.188	Rh
26	0.00021	353.039	352.834	0.205	Mylar
27	0.00292	352.834	350.471	2.363	Al-cat
28	0.00675	350.471	344.951	5.52	Al-deg
29	0.00031	344.951	344.759	0.192	Rh
30	0.00021	344.759	344.55	0.209	Mylar
31	0.00292	344.55	342.142	2.408	Al-cat
32	0.00675	342.142	336.515	5.627	Al-deg
33	0.00031	336.515	336.319	0.195	Rh
34	0.00021	336.319	336.105	0.214	Mylar
35	0.00292	336.105	333.649	2.456	Al-cat
36	0.00675	333.649	327.907	5.742	Al-deg
37	0.00031	327.907	327.708	0.199	Rh

Table 2.2 continued from previous page

38	0.00021	327.708	327.49	0.218	Mylar
39	0.00292	327.49	324.982	2.508	Al-cat
40	0.00675	324.982	319.118	5.864	Al-deg
41	0.00031	319.118	318.914	0.203	Rh
42	0.00021	318.914	318.691	0.223	Mylar
43	0.00292	318.691	316.129	2.563	Al-cat
44	0.00675	316.129	310.133	5.996	Al-deg
45	0.00031	310.133	309.925	0.208	Rh
46	0.00021	309.925	309.696	0.228	Mylar
47	0.00292	309.696	307.075	2.622	Al-cat
48	0.00675	307.075	300.937	6.137	Al-deg
49	0.00031	300.937	300.725	0.213	Rh
50	0.00021	300.725	300.491	0.234	Mylar
51	0.00292	300.491	297.805	2.685	Al-cat
52	0.00675	297.805	291.515	6.291	Al-deg
53	0.00031	291.515	291.297	0.218	Rh
54	0.00021	291.297	291.057	0.24	Mylar
55	0.00292	291.057	288.303	2.754	Al-cat
56	0.00675	288.303	281.846	6.457	Al-deg
57	0.00031	281.846	281.623	0.223	Rh
58	0.00021	281.623	281.376	0.247	Mylar
59	0.00292	281.376	278.547	2.829	Al-cat
60	0.00675	278.547	271.909	6.638	Al-deg
61	0.00031	271.909	271.679	0.229	Rh
62	0.00021	271.679	271.425	0.254	Mylar
63	0.00292	271.425	268.514	2.911	Al-cat
64	0.00675	268.514	261.677	6.837	Al-deg
65	0.00031	261.677	261.441	0.236	Rh
66	0.00021	261.441	261.179	0.262	Mylar
67	0.00292	261.179	258.177	3.002	Al-cat
68	0.00675	258.177	251.121	7.056	Al-deg
69	0.00031	251.121	250.878	0.244	Rh
70	0.00021	250.878	250.607	0.271	Mylar
71	0.00292	250.607	247.505	3.102	Al-cat
72	0.00675	247.505	240.205	7.3	Al-deg
73	0.00031	240.205	239.953	0.252	Rh
74	0.00021	239.953	239.672	0.281	Mylar
75	0.00292	239.672	236.459	3.213	Al-cat
76	0.00675	236.459	228.886	7.573	Al-deg
77	0.00031	228.886	228.625	0.261	Rh

Table 2.2 continued from previous page

78	0.00021	228.625	228.333	0.292	Mylar
79	0.000292	228.333	224.994	3.339	Al-cat
80	0.00675	224.994	217.111	7.882	Al-deg
81	0.00031	217.111	216.84	0.271	Rh
82	0.00021	216.84	216.535	0.305	Mylar
83	0.00292	216.535	213.053	3.482	Al-cat
84	0.00675	213.053	204.817	8.236	Al-deg

2.2.1 Detector Energy and Efficiency Calibration

In gamma ray spectrometry using Ge(Li) or HPGe detectors, one is generally interested in an initial calibration of an MCA which will determine the energy scale of pulse height distribution. This is called the energy calibration of the gamma ray spectrometry. What all is done for energy calibration is to place sources of know energy in front of the detector, record the spectrum for some time, then note the channel number into which the centroid of the resulting full energy peak falls. At least two energy points are required to determine the calibration curve, which essentially should be a straight line. However, other sources are often used to provide additional points along the straight line to test its linearity.

In the present work, it was observed that all the expected reaction products have their important characteristic gamma ray energies fall in the range upto 1000 kev. From this view point the energy calibration was done by using three well known standard radio active sources, ^{57}Co (122 keV), ^{137}Cs (662 keV) and ^{60}Co (1175 keV & 1332 keV). The linearity of the calibration curve was then checked by using a standard multi gamma ray source, ^{152}Eu and was found to be quite satisfactory.

Once the energy calibration or the spectrometer is over, the next step is to determine the efficiency of the detector using standard gamma ray sources. ^{152}Eu standard source has gained wide popularity because of its convenient half life (13 yrs.) and the wide range of gamma ray energies (100 to 1500 keV) produced in its decay. In employing a multi gamma ray source such a ^{152}Eu, extreme care must be taken to ensure that the measured peak intensities are not affected by sum coincidence effect, which occurs when two gamma rays emitted in coincidence from the source interact simultaneously in the detector, giving rise to a sum peak which may not correspond to either of the two full energy peaks. This problem is particularly severe for those sources that involve cascade gamma rays. One possible way to minimize these effects is to use small detector solid angles. For the present work, ^{152}Eu (Fig 2.1) standard source is adequate and hence taken for efficiency calibration, with due care being taken to avoid large solid angles. Some typical gamma ray energies of ^{152}Eu source selected for the efficiency calibration along with their abundance and uncertainties are give in Table 2.3.

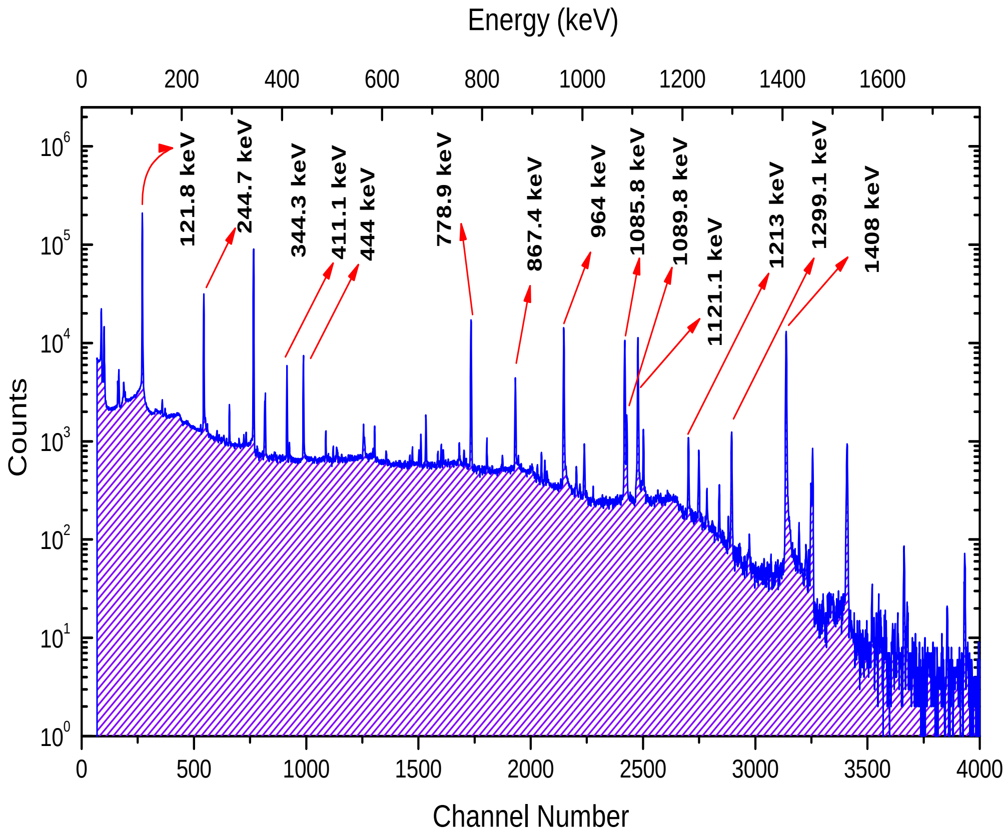

Figure 2.1: Measured gamma spectra of ^{152}Eu calibration source

Table 2.3: ^{152}Eu gamma ray energies, their abundances and uncertainties

Energy E_γ (keV)	Abundance I_γ (%)	Uncertainty in I_γ (%)
121.8	0.2837	0.83
244.7	0.0751	0.71
344.3	0.2658	0.68
778.9	0.1296	0.53
964	0.1462	0.4
1112.1	0.1356	0.41
1408.1	0.2085	0.4

The collected γ -ray spectra were analyzed by means of the ENCAMPLUS version 2.01 spectrum analysis software provided by Silena in combination with the spreadsheet program Excel. The ENCAMPLUS software was used for photopeak searches, area, statistical error calculations, background subtraction, and, in a few cases, multiple deconvolution where the photopeaks overlapped. The data sorting program EVAL of the data-acquisition system XSYS was used to extract the current integrator and timer scalar values from the event file logged during the experimental bombardment. The radionuclides produced in the ^{103}Rh target foils were identified by means of their characteristic gamma lines and their half-life by measuring the decrease of the activity with time. Table 2.4 gives the list of the identified isotopes, their half-life and spin, the energy and abundance of the characteristic γ-lines which were used. The decay data used in the analysis were taken from various literature [19–27].

Table 2.4: Identified isotopes, half-lives and spin, energies and abundancies of the characteristic gamma lines

Residue	Half-life (hrs.)	J^{π}	E_{γ} (keV)	Abundance (%)
^{94}Tc	4.883	7+	871.1	100
			702.6	99.6
			849.7	95.7
^{95}Tc	20	9/2+	765.8	93.82
^{96}Tc	102.72	7+	778.2	100
			849.9	98
			812.6	82
^{95}Ru	1.64	5/2+	336.4	70.2
^{97}Ru	69.6	5/2+	215.7	86
			324.5	10.79
^{97}Rh	0.512	9/2+	421.6	75
^{99}Rh	386.4	1/2-	528.2	38
			353.1	34.6
^{101}Rh	104.2	9/2+	306.9	81
			545	4.27
^{99}Pd	0.357	5/2+	136	73
^{100}Pd	87.12	0+	126.1	7.8
^{101}Pd	8.47	5/2+	296.3	19
			590.4	12.06
^{103}Ag	1.095	7/2+	118.7	31.2
			148.1	28.3
			266.9	13.3
^{104}Ag	1.153	5+	555.8	92.6
			767.7	65.7
^{105}Ag	990.96	1/2-	344.5	41
			280.4	30.2
			443.4	10.5
			644.6	11.1
^{104}Cd	0.962	0+	709.6	19.5

2.2.2 Determination of the Reaction Cross-section

Expression for constant beam intensity

The activity at the middle-value of a measurement period is given by

$$\frac{dN}{dt} = \lambda\, N = \frac{A_p}{\tau \upsilon \delta} = \lambda\, I_t \sigma\, N_0 \tag{2.1}$$

where
λ is the decay constant of the particular radionuclide, A_p is the photopeak area of a particular γ-ray line, τ is the live counting time, υ is the branching ratio (intensity) of the gamma line, δ is the efficiency of the detector, N is total number of radioactive nuclei produced, N_0 is the total number of target nuclei per unit area, I_t is the total number of beam particles accumulated on the target during bombardment, and σ is the production cross-section.

We now define the following times:
$t = 0$ BOB (beginning of bombardment),
$t = t_1$ EOB (end of bombardment),
$t = t_2$ beginning of counting period),
$t = t_3$ end of counting period.
Thus, the decay time between EOB and start of counting is $t_2 - t_1$, and the live counting time is given by $t_3 - t_2$. We also have the following relation:

$$t_3 - t_2 = \tau + \Delta\tau, \tag{2.2}$$

where $\Delta\tau$ is the dead time of the counting system.

For the sake of mathematics it is convenient to divide the irradiation time into n small increments of Δt:

$$\Delta t = \frac{t_1}{n} \tag{2.3}$$

The activity produced in each incremental period Δt is therefore

$$\frac{\lambda I_t \sigma N_0}{n} = \frac{\lambda I_t \sigma N_0 \Delta t}{t} \tag{2.4}$$

Projected to EOB, this activity is given by

$$\Delta A_i = \frac{\lambda I_t \sigma N_0 \Delta t}{t_1} e^{-\lambda(t_1 - i\Delta t)} \quad for \quad 1 \leqslant i \leqslant n. \tag{2.5}$$

The total activity at EOB is therefore given by

$$\begin{aligned}
A_{EOB} = A(t_1) &= \lim_{n\to\infty}\sum_{i=1}^{n}\Delta A_i \\
&= \frac{\lambda I_t \sigma N_0}{t_1}\lim_{n\to\infty}\sum_{i=1}^{n} e^{-\lambda(t_1 - i\Delta t)}\,\Delta t \\
&= \frac{\lambda I_t \sigma N_0}{t_1}\int_0^{t_1} e^{-\lambda(t_1-t)}\,dt \\
&= \frac{\lambda I_t \sigma N_0}{t_1}\left[\frac{e^{-\lambda(t_1-t)}}{\lambda}\right]_0^{t_1} \\
&= \frac{I_t \sigma N_0}{t_1}\left[1 - e^{-\lambda t_1}\right]. \qquad (2.6)
\end{aligned}$$

Decay during period t_1 to t_2

$$A(t_2) = A(t_1)\,e^{-\lambda(t_2-t_1)} \qquad (2.7)$$

To calculate decay during counting period

$$\begin{aligned}
A(t_2)\,e^{-\lambda t_m} &= \frac{1}{(t_3-t_2)}\int_{t_3}^{t_2} A(t)\,dt \\
&= \frac{1}{(t_3-t_2)}\int_{t_3}^{t_2} A(t_2)\,e^{-\lambda t}dt \\
\therefore e^{-\lambda t_m} &= \left[\frac{e^{-\lambda t}}{-\lambda(t_3-t_2)}\right]_{t_3}^{t_2} = \frac{e^{-\lambda t_3} - e^{-\lambda t_2}}{-\lambda(t_3-t_2)} \\
\therefore t_m &= -\frac{1}{\lambda}\ln\left\{\frac{e^{-\lambda t_3} - e^{-\lambda t_2}}{-\lambda(t_3-t_2)}\right\}, \quad \text{and} \qquad (2.8)
\end{aligned}$$

$$A(t_m) = A(t_2)\,e^{-\lambda(t_m-t_2)}. \qquad (2.9)$$

From Eq. 2.7 and Eq. 2.9 we can write:

$$\begin{aligned}
A(t_m) &= A(t_1)\,e^{-\lambda(t_2-t_1)}\,e^{-\lambda(t_m-t_2)} \\
&= A(t_1)\,e^{-\lambda(t_m-t_1)}. \qquad (2.10)
\end{aligned}$$

Substituting from Eqs. 2.6 and 2.1:

$$A(t_m) = \frac{I_t \sigma N_0}{t_1}\left[1 - e^{-\lambda t_1}\right] e^{-\lambda(t_m-t_1)} = \frac{A_p}{\tau \upsilon \delta}. \qquad (2.11)$$

Let all times be in seconds and N_0 be the number of traget nuclei per cm^2. Then taking into account that $1\ mb = 1 \times 10^{-27} cm^2$, Eq. 2.11 can be reorganized to give the cross-sections:

$$\sigma(\,mb) \;=\; \frac{A_p t_1}{\tau v \delta I_t N_0(\,1 - e^{-\lambda t_1}\,)\, e^{-\lambda(\,t_m - t_1)}\,(\,1 \times 10^{-27})} \tag{2.12}$$

In the above equation, the total number of incident beam particles can be calculated as:

$$I_t = \frac{Q \times 10^{-9}}{q_e \times m}, \tag{2.13}$$

where

Q = total charge integrated on target (nC),
q_e = 1.602177×10^{-19} = charge of electron,
m = charge state of beam particles.

and the total number of target nuclei per cm^2 can be calculated as:

$$N_s = \frac{(\,\rho s)\, N_A}{M_a}, \tag{2.14}$$

where

ρ = density of target foil (g/cm^3),
s = foil thickness (cm),
ρs = areal thickness (g/cm^2),
N_A = Avogadro's number = $6.022136 \times 10^2 3$,
M_a = atomic mass of foil material (AMU).

Expression for fluctuating beam intensity

When the beam intensity fluctuates during the bombardment, it is possible that the expressions derived above may yield inaccurate result, especially for isotopes with half lives shorter than or of the same order as the bombardment time. It is possible to make a correction for the effect of fluctuations. In the near target residue experiment we logged the integrated beam current every 10 seconds. We will now derive the expressions similar it those described above, but using the logged information of the integrated beam current.

Let

t = 0 BOB (beginning of bombardment),
Δt = 10 s increment of current integrator scaler,
n = total number of 10 s time increments in bombardment period,
$n\Delta t$ = EOB (end of bombardment).

Then the end of each time interval is given by

$$h_i = i\Delta t \qquad for \qquad 1 \leqslant i \leqslant n.$$

The activity produced in each time interval, assuming that the half-life is much larger than the incremental time interval of 10 s, is given by

$$\Delta A_i = \lambda N_0 \sigma \Delta I_i \qquad for \qquad 1 \leqslant i \leqslant n. \tag{2.15}$$

where λ, N_0 and σ have the same meanings as before, and ΔI_i is the total number of particles incident on the target on the i^{th} time increment. Similar to Eq. 2.13, the number of incident beam particles per time increment is given by

$$\Delta I_i = \frac{\Delta Q_i \times 10^{-9}}{q_e \times m}, \tag{2.16}$$

where q_e and m have the same meanings as before, and ΔQ_i is the charge accumulated (nC) in the i^{th} time increment. These ΔQ_i values have been written to hard disk in the data room during the foil stack irradiations.

Let t_{ref} be any convenient reference time after EOB. Then the incremental activity at the reference time is given by

$$\Delta A_i(t_{ref}) = \Delta A_i e^{-\lambda(t_{ref}-h_i)}. \tag{2.17}$$

The total activity at the reference time is then given using Eqs. 2.15 and 2.17, as

$$\begin{aligned} A(t_{ref}) &= \sum_{i=1}^{n} \Delta A_i(t_{ref}) \\ &= \sum_{i=1}^{n} \Delta A_i e^{-\lambda(t_{ref}-h_i)} \\ &= \lambda N_0 \sigma \sum_{i=1}^{n} \Delta I_i e^{-\lambda(t_{ref}-h_i)} \end{aligned} \tag{2.18}$$

Let $t = t_2$ be the start of the counting period and $t = t_3$ be the end of the counting period, and τ be the live counting time. As before (Eq. 2.8) we define t_m, $t_2 \leq t_m \leq t_3$, so that the instantaneous activity at t_m equals the average activity over the counting period. Then the total activity at $t = t_m$ is given by

$$A(t_m) = \frac{A_p}{\tau v \delta}, \tag{2.19}$$

where A_p, v and δ have the same meanings as before. Now we deliberately choose $t_{ref} = t_m$, therefore $A(t_{ref}) = A(t_m)$, and from Eqs. 2.18 and 2.19 we immediately get

$$\lambda N_0 \sigma \sum_{i=1}^{n} \Delta I_i e^{-\lambda(t_m - h_i)} = \frac{A_p}{\tau v \delta},$$

therefore

$$\sigma = \frac{A_p}{\lambda N_0 \tau v \delta \sum_{i=1}^{n} \Delta I_i e^{-\lambda(t_m - h_i)}}. \tag{2.20}$$

The units in Eq. 2.20 will be cm^2, so we can convert to mb as before:

$$\sigma(mb) = \frac{A_p}{\lambda N_0 \tau v \delta (1 \times 10^{-27}) \sum_{i=1}^{n} \Delta I_i e^{-\lambda(t_m - h_i)}}. \tag{2.21}$$

Correction factor for constant beam intensity assumption

Eqs. 2.12 and 2.21 have been derived for the cross-section, with Eq. 2.21 clearly more general and therefore the desirable formula to use if it is known that the beam intensity fluctuations was not negligible. Alternatively, we may prefer to use Eq. 2.12 due to its simplicity and seek to calculate a correction factor due to beam intensity fluctuations. We will now proceed to derive this correction factor. Let's assume that the cross-section of Eq. 2.12 has to be multiplied with a factor K in order to arrive at the same answer as given by Eq. 2.21. Hence

$$K \left[\frac{A_p t_1}{\tau v \delta I_t N_0 (1 - e^{-\lambda t_1}) e^{-\lambda(t_m - t_1)} (1 \times 10^{-27})} \right] = \frac{A_p}{\lambda N_0 \tau v \delta (1 \times 10^{-27}) \sum_{i=1}^{n} \Delta I_i e^{-\lambda(t_m - h_i)}}$$

$$\therefore \frac{K t_1}{I_t (1 - e^{-\lambda t_1}) e^{-\lambda(t_m - t_1)}} = \frac{1}{\lambda \sum_{i=1}^{n} \Delta I_i e^{-\lambda(t_m - h_i)}} \tag{2.22}$$

A little algebra later (t_m can be eliminated, as expected) one gets for K:

$$K = \frac{\left(\sum_{i=1}^{n} \Delta I_i \right) (e^{\lambda t_1} - 1)}{\lambda t_1 \left(\sum_{i=1}^{n} \Delta I_i e^{-\lambda t_i} \right)} \tag{2.23}$$

Eq. 2.23 was evaluated for all the relevant foil-stack irradiations, where K was simply considered to be a function of the half-life. As one can expect,

K does not show any specific functional form which can be parameterised because fluctuations in beam intensity can be very unpredictable. The best way to find the correction for a specific case is to use calculated tabled values and interpolate.

So,finally, the experimental production cross sections were obtained from the photopeak area extracted from the measured gamma spectra by means of the following expressions:

$$\sigma\left(mb\right) = \left(A_p T_1 K\right) / \left(\tau v \delta I_t N_0 exp\left[-\lambda\left(T_m - T\right)\right]\right) \times \\ \left[1 - exp\left(-\lambda T_1\right)\right]\left(1 \times 10^{-27}\right),$$

where A_p is the photopeak area of a particular γ-ray line, $t = T_1$ is the duration of the bombardment where $t = 0$ is taken as the start time of bombardment, K is a correction factor for beam intensity fluctuations, τ is the live counting time, v is the branching ratio (intensity) of the gamma line, δ is the efficiency of the detector, I_t is the total number of beam particles accumulated on the target during bombardment, N_0 is the total number of target nuclei per unit area, λ is the decay constant of the particular radionuclide, and T_m is the mean value of the measuring counting interval. All times have units of seconds, and the result of the above equation is given in units of millibarns (mb)(Table 2.5, 2.6, 2.7). The factor K is given by

$$K = \frac{\left(\sum_{i=1}^{n} \Delta I_i\right)\left[exp(\lambda T_1) - 1\right]}{\lambda T_1 \sum_{i=1}^{n} \Delta I_i exp(-\lambda h_i)},$$

where n is the number of current integrator readings logged during the bombardment period (scalar values were logged every 10 s), ΔI_i is the beam current integrated (or the number of beam particles on target) during the i^{th} time increment (of 10-s duration) during the bombardment $1 \leq i \leq n$, and $t = h_i$ is the end of each time increment since the start of the bombardment. Finally, the mean-value time of counting is given by

$$T_m = -\frac{1}{\lambda} \ln\left[\frac{exp\left[-\lambda\left(T_3 - T_2\right)\right]}{-\lambda\left(T_3 - T_2\right)}\right],$$

where $t = T_2$ denotes the start time of the counting period and $t = T_3$ denotes the end time of the counting period, relative to $t = 0$ being the start time of the bombardment.

The factor K may become important whenever the half-life of a particular radionuclide is shorter than or on the same order of magnitude as the bombardment time. In such cases, K can be strongly dependent on fluctuations in the beam intensity and become different from a normative value of unity.

Table 2.5: Measured cross sections of ^{103}Ag, ^{104}Ag, ^{105}Ag, ^{104}Cd, ^{99}Pd residues formed in the interaction of ^{14}N with ^{103}Rh upto 400 MeV

Energy (MeV)	σ (mb)				
	^{103}Ag	^{104}Ag	^{105}Ag	^{104}Cd	^{99}Pd
89.4	12.8 ± 1.4	9.32 ± 1.2	8.0 ± 2.3		
110.9	122 ± 13.4	20.3 ± 4.0	24.7 ± 3.2	27.5 ± 5.3	
129.7	228 ± 27.4	32.3 ± 4.3	55.9 ± 8.4	45.8 ± 6.8	
146.7	15.6 ± 3.2	20.7 ± 1.2	223 ± 24.5	30.3 ± 4.1	6.13 ± 0.78
162.3	44.8 ± 8.9	103 ± 7.3	331 ± 36.5	45.4 ± 4.5	8.13 ± 1.14
176.8	55.3 ± 10.5	146 ± 11.8	389 ± 38.6	64.2 ± 6.6	9.06 ± 1.26
190.5	83.2 ± 15.8	130 ± 9.1	310 ± 34.1	105 ± 13.8	26.5 ± 2.9
203.5	102 ± 8.6	132 ± 6.2	241 ± 28.9	110 ± 14.3	33.4 ± 4.0
215.8	96.1 ± 10.8	116 ± 4.6	203 ± 24.6	137 ± 13.8	41.2 ± 4.7
227.7	94.8 ± 5.7	91.5 ± 3.3	170 ± 19.7	117 ± 14.8	32.3 ± 3.8
239	124 ± 4.3	87.8 ± 3.3	146 ± 12.8	120 ± 15.2	40.5 ± 5.2
250	134 ± 9.8	77.5 ± 3.6	114 ± 10.9	114 ± 15.1	53.4 ± 7.0
250.9	145 ± 9.6	56.5 ± 2.4	111 ± 10.2	104 ± 13.6	52.8 ± 7.2
261.7	133 ± 15.9	49.1 ± 2.2	116 ± 10.8	107 ± 14.2	50.5 ± 6.5
271.9	84.1 ± 5.0	28.2 ± 2.8	126 ± 11.3	114 ± 13.9	44.5 ± 6.0
281.8	63.0 ± 11.4	20.0 ± 1.0	49.8 ± 5.4	97.8 ± 10.9	45.7 ± 5.5
291.5	71.9 ± 15.4	19.3 ± 1.6	61.4 ± 5.5	61.7 ± 8.1	38.9 ± 5.5
300.9	57.3 ± 15.3	17.1 ± 1.7	52.7 ± 5.1	50.9 ± 7.0	45.4 ± 6.7
310.1	50.7 ± 11.6	16.2 ± 1.6	31.4 ± 3.2	40.8 ± 5.2	36.4 ± 4.9
319.1	45.0 ± 13.5	12.6 ± 1.5	27.6 ± 3.6	32.4 ± 4.6	38.4 ± 5.4
327.9	39.1 ± 8.3	9.9 ± 1.3	32.1 ± 3.8	30.9 ± 4.4	28.5 ± 4.4
336.5	38.8 ± 8.2	9.9 ± 0.8	23.6 ± 3.0	35.3 ± 6.2	27.6 ± 3.6
344.9	31.9 ± 7.0	9.3 ± 1.4	25.2 ± 3.1	26.9 ± 5.8	23.5 ± 3.6
353.2	34.0 ± 7.1	7.7 ± 1.1	23.1 ± 2.7	28.7 ± 7.0	24.0 ± 3.8
361.4	25.0 ± 5.7	6.4 ± 0.8	31.2 ± 3.4	29.2 ± 5.9	23.4 ± 3.9
369.3	28.4 ± 6.1	6.9 ± 1.0	32.2 ± 3.3	22.1 ± 4.9	17.6 ± 3.4
377.2	20.8 ± 9.6	6.3 ± 0.7	23.9 ± 2.9	22.6 ± 4.5	107 ± 19.2
384.9	21.1 ± 5.0	6.7 ± 1.5	17.9 ± 2.0	22.5 ± 4.5	118 ± 22.4
392.5	22.1 ± 5.1	7.9 ± 1.3	24.7 ± 2.9	19.3 ± 3.7	150 ± 28.5
400	20.7 ± 4.2	6.4 ± 1.2	11.5 ± 2.1	18.8 ± 3.8	

Table 2.6: Measured cross sections of ^{100}Pd, ^{101}Pd, ^{97}Rh, ^{99}Rh, ^{101}Rh residues formed in the interaction of ^{14}N with ^{103}Rh upto 400 MeV

Energy	σ (mb)				
(MeV)	^{100}Pd	^{101}Pd	^{97}Rh	^{99}Rh	^{101}Rh
89.4	9.32 ± 1.2	8.0 ± 2.3			
110.9	24.7 ± 3.2	27.5 ± 5.3			35.1 ± 4.2
129.7	55.9 ± 8.4	45.8 ± 6.8			80.2 ± 9.6
146.7	87.6 ± 12.9	71.8 ± 8.5		11.0 ± 1.5	113 ± 15.8
162.3	135 ± 18.9	143 ± 11.9		39.5 ± 4.8	149 ± 19.4
176.8	166 ± 21.6	190 ± 13.8		60.7 ± 9.5	252 ± 35.1
190.5	234 ± 28.5	204 ± 14.3	9.9 ± 1.2	78.7 ± 11.4	314 ± 33.6
203.5	256 ± 31.7	218 ± 14.8	20.6 ± 2.3	94.7 ± 12.3	388 ± 46.6
215.8	293 ± 35.2	221 ± 14.8	19.4 ± 2.5	148 ± 13.7	348 ± 38.3
227.7	287 ± 34.4	230 ± 15.2	23.4 ± 3.2	162 ± 15.4	351 ± 45.6
239	326 ± 35.9	228 ± 15.1	37.5 ± 4.8	171 ± 18.9	375 ± 41.3
250	171 ± 25.6	184 ± 13.6	36.6 ± 4.7	165 ± 15.3	357 ± 42.8
250.9	131 ± 18.3	202 ± 14.2	29.4 ± 3.5	146 ± 19.7	311 ± 33.5
261.7	190 ± 22.8	195 ± 13.9	41.7 ± 5.7	170 ± 23.1	329 ± 46.1
271.9	112 ± 16.8	141 ± 11.9	48.6 ± 6.7	254 ± 27.9	314 ± 33.9
281.8	188 ± 22.6	164 ± 12.8	37.4 ± 5.5	188 ± 21.7	313 ± 34.4
291.5	129 ± 19.4	145 ± 12.0	58.7 ± 8.7	187 ± 26.2	348 ± 31.3
300.9	179 ± 23.3	141 ± 11.9	52.5 ± 9.3	167 ± 23.4	330 ± 33.0
310.1	115 ± 16.1	124 ± 11.1	60.2 ± 11	171 ± 25.6	303 ± 33.3
319.1	91.3 ± 13.9	142 ± 11.9	48.9 ± 5.8	149 ± 14.6	281 ± 33.7
327.9	152 ± 25.9	142 ± 11.9	50.2 ± 8.0	150 ± 17.9	263 ± 34.2
336.5	156 ± 26.5	129 ± 11.4	53.1 ± 7.4	175 ± 24.5	283 ± 33.9
344.9	123 ± 20.9	121 ± 11.0	52.0 ± 11	153 ± 19.9	264 ± 42.2
353.2	153 ± 30.6	113 ± 10.6	53.7 ± 11	150 ± 24.2	267 ± 37.4
361.4	121 ± 19.4	129 ± 11.3	45.7 ± 5.5	165 ± 23.1	233 ± 34.9
369.3	133 ± 23.9	107 ± 10.3	46.6 ± 12	129 ± 21.9	244 ± 39.0
377.2	107 ± 19.2	109 ± 10.4	41.6 ± 3.8	130 ± 22.8	201 ± 33.6
384.9	118 ± 22.4	94.0 ± 9.7	44.6 ± 15	139 ± 24.7	216 ± 32.1
392.5	150 ± 28.5	95.8 ± 9.8	40.1 ± 8.3	142 ± 26.9	209 ± 29.3
400			41.6 ± 5.4	107 ± 17.1	124 ± 14.9

Table 2.7: Measured cross sections of ^{95}Ru, ^{97}Ru, ^{94}Tc, ^{95}Tc, ^{96}Tc residues formed in the interaction of ^{14}N with ^{103}Rh upto 400 MeV

Energy	σ (mb)				
(MeV)	^{95}Ru	^{97}Ru	^{94}Tc	^{95}Tc	^{96}Tc
89.4					
110.9					
129.7					
146.7		20.7 ± 2.7			
162.3		18.5 ± 2.4	3.7 ± 0.6	2.7 ± 0.05	
176.8		34.2 ± 5.5	5.0 ± 0.8	6.5 ± 0.1	
190.5	14.5 ± 2.0	63.7 ± 8.9	7.1 ± 1.3	13.2 ± 0.3	13.3 ± 2.4
203.5	16.4 ± 2.8	82.4 ± 12.3	11.2 ± 2.1	23.9 ± 0.6	19.1 ± 3.1
215.8	20.6 ± 3.9	105 ± 13.9	16.8 ± 3.5	34.1 ± 0.8	23.3 ± 5.3
227.7	22.0 ± 3.8	147 ± 14.7	17.4 ± 5.4	51.5 ± 1.3	30.2 ± 4.2
239	41.0 ± 7.0	150 ± 16.5	21.6 ± 7.1	73.9 ± 1.9	35.0 ± 4.1
250	39.3 ± 6.1	182 ± 20.0	17.7 ± 4.4	96.6 ± 2.5	36.8 ± 2.1
250.9	31.2 ± 5.1	131 ± 20.9	16.3 ± 3.3	117 ± 2.7	32.2 ± 6.1
261.7	45.9 ± 5.7	154 ± 18.6	22.6 ± 4.1	68.9 ± 1.6	34.3 ± 6.5
271.9	56.5 ± 7.0	228 ± 31.9	30.7 ± 7.4	98.5 ± 2.4	40.9 ± 8.6
281.8	57.5 ± 7.9	191 ± 28.7	30.4 ± 3.9	111 ± 2.8	37.1 ± 6.3
291.5	53.2 ± 7.5	252 ± 45.4	38.7 ± 8.4	100 ± 2.6	43.3 ± 8.2
300.9	56.8 ± 7.9	224 ± 42.5	44.6 ± 7.5	134 ± 4.3	39.5 ± 7.1
310.1	61.5 ± 8.0	247 ± 29.6	49.1 ± 6.9	141 ± 4.1	42.4 ± 6.4
319.1	65.2 ± 8.4	208 ± 33.3	71.3 ± 11.1	150 ± 4.0	43.2 ± 8.5
327.9	63.0 ± 9.5	235 ± 28.2	70.7 ± 9.9	157 ± 5.9	53.6 ± 8.5
336.5	68.4 ± 9.6	242 ± 26.6	59.7 ± 4.9	152 ± 5.7	45.5 ± 5.0
344.9	75.9 ± 12.1	255 ± 33.2	79.7 ± 10.9	173 ± 4.2	53.0 ± 4.0
353.2	78.5 ± 10.2	236 ± 40.1	68.3 ± 8.8	182 ± 5.7	59.0 ± 3.6
361.4	76.1 ± 16.0	241 ± 43.4	70.5 ± 6.8	183 ± 5.8	46.5 ± 1.6
369.3	81.7 ± 13.8	229 ± 43.5	91.7 ± 10.8	168 ± 3.4	55.2 ± 2.7
377.2	79.9 ± 15.2	210 ± 37.8	86.3 ± 6.1	187 ± 6.4	49.2 ± 9.2
384.9	78.1 ± 17.9	188 ± 37.6	79.1 ± 10.5	160 ± 5.1	58.4 ± 2.5
392.5	83.4 ± 18.3	205 ± 45.1	59.8 ± 8.0	165 ± 5.1	61.4 ± 2.4
400	75.8 ± 15.9	169 ± 32.1	56.7 ± 8.5	162 ± 4.8	56.2 ± 1.8

2.2.3 Errors in the Cross-section Measurement

Considering the various sources of errors, including the uncertainty in target thickness, in the beam fluence measurement, the HPGe detector efficiency, the counting efficiency due to electronics dead time and the statistical errors in evaluating the γ-line intensity and the background subtraction, the uncertainty values of the experimental cross sections were estimated to be typically between 15% and 20%.

2.3 Model Calculations

Theoretical calculations were performed using the latest (at the time of data analysis) released computer code ALICE2014 [11–13,16–18]. This nuclear reaction code is the latest version of the so-called HMS-ALICE codes in which pre-equilibrium emission of both nucleons and light clusters is based on the HMS model [17]. All cascades are terminated according to the Weisskopf-Ewing evaporation model [28], and the equilibrium emission of both nucleons and light clusters can be selected. The options for emission were taken to be similar, *i.e.*, for both pre-equilibrium as well as equilibrium emission of n, p, ^2H, ^3H, ^3He and ^4He were chosen for the present calculations. Calculations were performed with three forms of the nuclear level density: Kataria-Ramamurthy and Kapoor [29] (KR), Obninsk [30] (OB), and backshifted Fermi gas (FG). The OB and KR forms do not have any adjustable parameters. For FG we performed the calculations with level density parameter "a" $= A/9$, which is the default value. The changes resulting in varying a in the range of $A/7 - A/11 MeV^{-1}$ is 10% or less throughout the energy region. Fig-2.2 shows the variation in level density as a function of excitation energy. The other input parameters were set to the default values of the code. Further details of the code are available in the literature [11–16] and Chapter 1.

2.3.1 Level Density Analysis

The absolute values of level density are vastly different. This is illustrated in Fig-2.12 for one case. It will be noticed that at 200-MeV excitation, the OB level density is 20 orders of magnitude less than the FG level density with $a = A/7 MeV^{-1}$, however, it is the excitation energy dependence that matters and not the absolute value of the level density. As seen in the Fig-2.12, the OB level density has a distinctly different energy dependence as compared to the other level-density forms. It is important to note that in the original formulation of the KR level density [29] excitation energies above

60 MeV were not considered. For higher excitation the FG ($a = A/9MeV^{-1}$) level-density form scaled to the 60-MeV KR value is used in ALICE2014. The OB level density was formulated relatively recently as compared to FG and KR, and it is heartening to note that overall it performs better in comparison with the present data. It is true that specific cases show differing degrees of agreement in different energy ranges, however, this is only to be expected for calculations of a global nature without adjustable parameters.

As already mentioned earlier, varying the value of the FG level-density parameter between $A/7$ and $A/11MeV^{-1}$ only results in small changes. As an example of this insensitivity, Fig-2.2 shows calculations using $a = A/7, A/9andA/11$ for the excitation function of the ^{100}Pd residue. Consequently, a value of $A/9$ was adopted throughout for the remainder of the calculations.

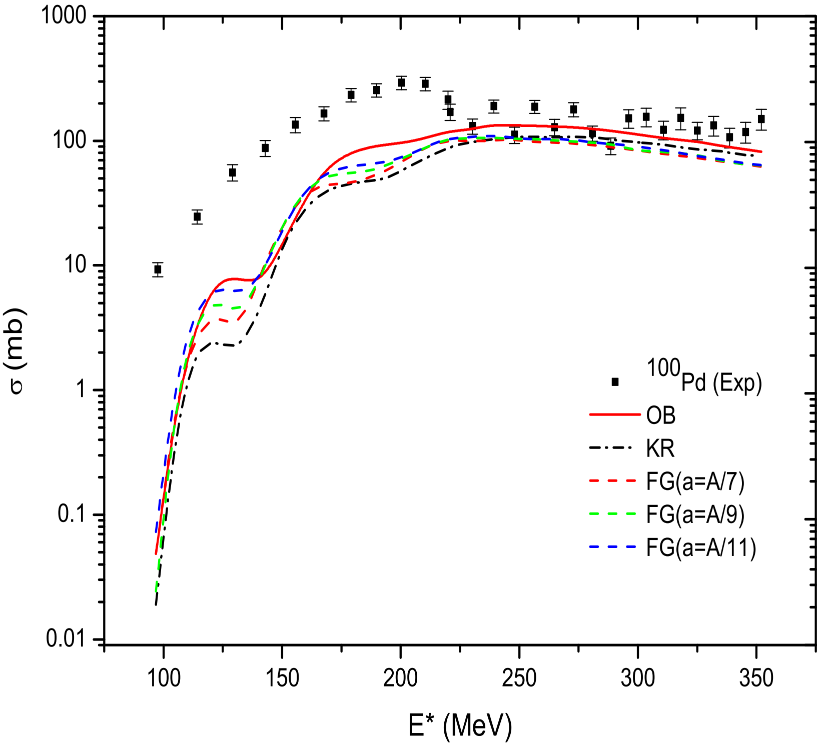

Figure 2.2: Excitation function ^{100}Pd residue in the ^{14}N+^{103}Rh reaction with different level-density options.

2.4 Results and Discussion

The experimental cross sections are presented in Tables 2.5 to 2.7 and are compared with the ALICE2014 theoretical predictions in Figures 2.3 to 2.8. The calculated excitation functions are shown as dashed curves (using Obninsk level densities), solid curves (using Fermi gas level densities), and dashed-dotted curves (using Kataria-Ramamurthy level densities). In the case of cumulative cross sections for the formation of the observed residues, the fractional contributions from precursor decay were summed to the directly produced contribution. These fractional precursor contributions were obtained by adopting the procedure given in the literature [1,2].

The silver residues observed in this paper are $^{103-105}Ag$, shown in Fig-2.3. The experimental excitation function of ^{103}Ag exhibits a broad peak with a maximum of 145 mb at 250.9 MeV, beyond which the slope of the curve decreases monotonically towards higher energies. The excitation functions of ^{104}Ag and ^{105}Ag show similar trends, reaching maxima of 146 and 389 mb at 176.8 MeV, respectively. The theoretical predictions with all three level-density formalisms (OB, FG, and KR) are reasonable in the case of the ^{103}Ag isotope. In the case of $^{104,105}Ag$, both FG and KR give a better agreement than the OB level density, above 250 MeV. A more pronounced underprediction is consistently observed with all three level densities below 250MeV. However, the discrepancy is more pronounced in the case of FG and KR as compared to the OB level density for $^{104,105}Ag$ isotopes.

The only residue of cadmium observed in this paper is ^{104}Cd, shown in Fig-2.4. Here the calculations with all three level-density formalisms show nearly identical results, which are quite close to the data. The excitation function is rather structureless and almost constant between 200 and 300 MeV. The measurements seem to support the three local maxima predicted by the calculations but shifted towards higher energies. The experimental maximum is 137 mb at 215.8 MeV. Both the FG and the OB level densities give similar results in the entire energy region, whereas the KR level density underestimates the experimental results below 150 MeV.

The observed palladium residues are $^{99-101}Pd$, shown in Fig-2.5. The shapes of these excitation functions are also quite structureless, rising rather gently from their respective thresholds to exhibit very broad peaks. Beyond the peak maxima, the decreasing trend of the excitation functions is quite small, thus their appearance seems almost flat towards higher energies. The calculations show a marked underprediction towards lower energies in the cases of ^{100}Pd and ^{101}Pd. This discrepancy is not observed in the case of ^{99}Pd, however, an overprediction is evident towards higher energies for both OB and FG level densities. The overall agreement with the measurements is markedly better when using the OB level density in comparison with those given by FG and KR.

The excitation functions for the $^{97,99,101}Rh$, $^{95,97}Ru$, and $^{94-96}Tc$ residues exhibit very similar trends as shown in Figures 2.6 to 2.8. No prominent peaks or local maxima are observed. Rather, the excitation functions rise from their respective thresholds up to nearly constant plateaus towards higher energies. The theoretical calculations reproduce the plateaus very satisfactorily when the OB level densities are used. In contrast, rather serious underpredictions are evident in some of the cases, that is, Rh, Ru, and Tc isotopes where FG and KR level-density options are used. Overall in the above-mentioned three sets of isotopes, OB gives by far the best agreement in comparison with the FG and KR options of level density.

Figures 2.9 to 2.11 show the comparison of three of the presently measured excitation functions ($^{14}N+^{103}Rh$) with those measured earlier for the systems of ^{12}C and $^{16}O+^{103}Rh$ up to 400 MeV [1–3]. Same global parameters were used in the HMS model calculations in all three systems.

Three typical excitation functions for the residues, ^{94}Tc, ^{99}Rh, and ^{100}Pd were selected for intercomparison of the systems with the present HMS model calculations. In Fig-2.9, it may be observed that the excitation function for ^{94}Tc gives the best results for the OB level density for the $^{12}C+^{103}Rh$ system between 200 and 400 MeV, whereas for $^{14}N+^{103}Rh$ the results are better with the OB level densities between 250 and 400 MeV. In the case of $^{16}O+^{103}Rh$, there is a gross underestimation by all three level densities. In the case of the excitation function of ^{99}Rh (Fig-2.10), both ^{12}C and $^{14}N+^{103}Rh$ systems give similar and best results with the OB level density, whereas for the $^{16}O+^{103}Rh$ system the calculations underestimate the experimental results. In Fig-2.11, $^{12}C+^{103}Rh$ gives the best agreement with all three level densities (OB, KR, and FG) as compared to the ^{14}N and $^{16}O+^{103}Rh$ systems. In general, it may be concluded that the present theoretical and experimental results are quite close in agreement with the $^{12}C+^{103}Rh$ system, whereas for the $^{16}O+^{103}Rh$ system the theoretical results significantly underestimate the experimental results.

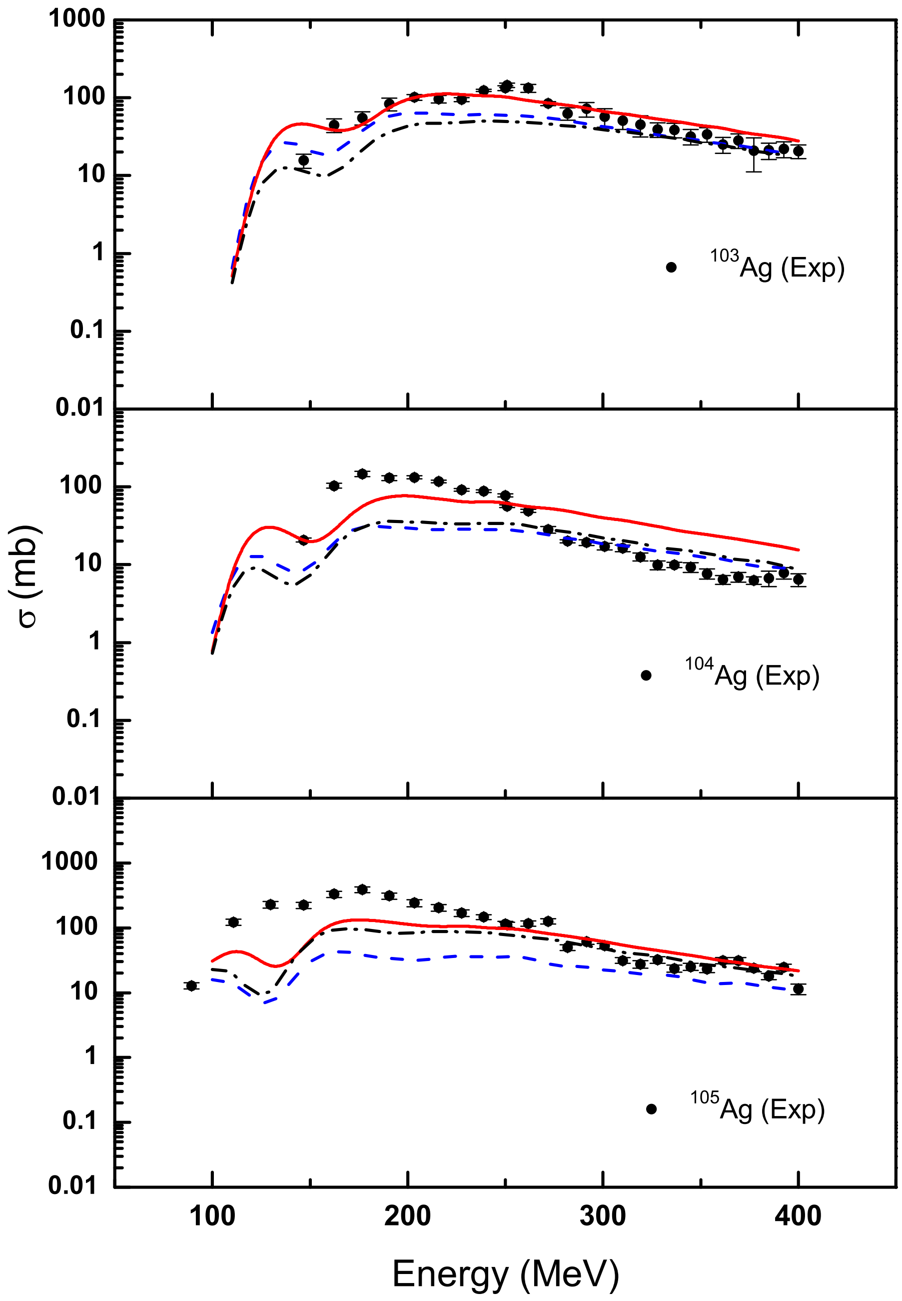

Figure 2.3: Excitation functions of Ag residues formed in the interaction of ^{14}N with ^{103}Rh as indicated. The solid symbols are the experimental results of this paper. The calculated excitation functions are shown as the red solid curves (OB level density), the blue dashed curves (FG level density), and the black dashed-dotted curves (KR level density) as obtained with the nuclear reaction code ALICE2014.

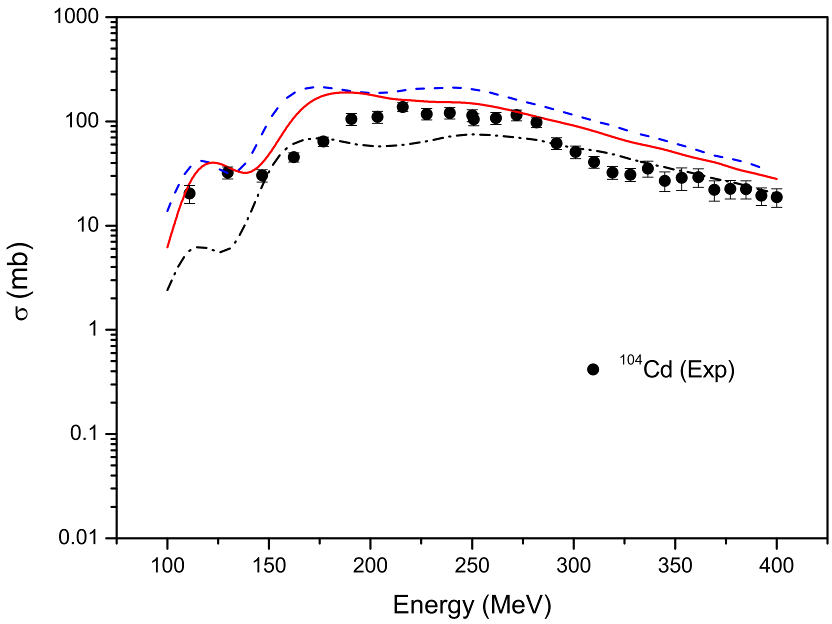

Figure 2.4: Excitation function of ^{104}Cd residues formed in the interaction of ^{14}N with ^{103}Rh. Also see the caption for Fig.2.3 for more details.

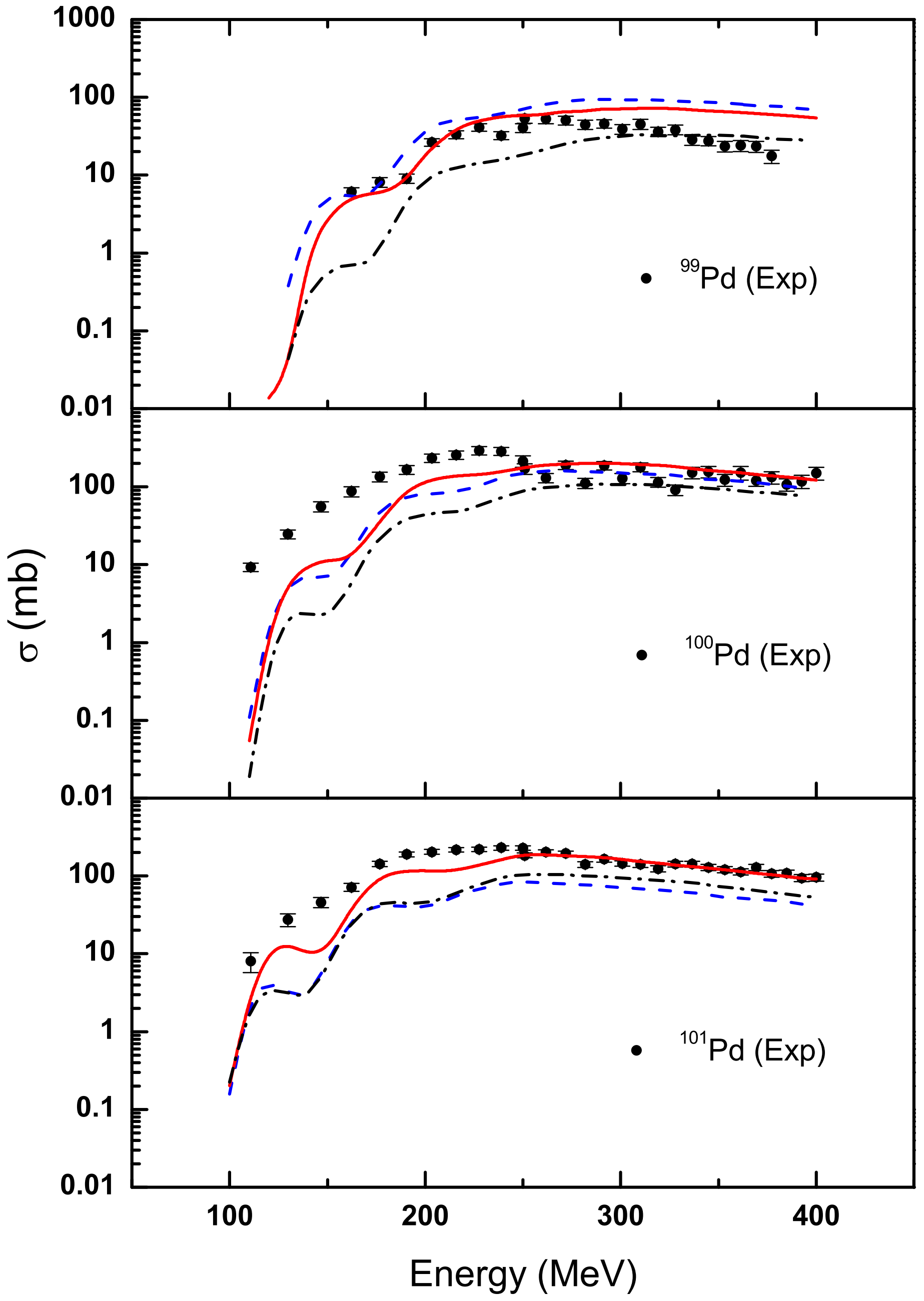

Figure 2.5: Excitation function of *Pd* residues formed in the interaction of ^{14}N with ^{103}Rh as indicated. Also see the caption for Fig.2.3 for more details.

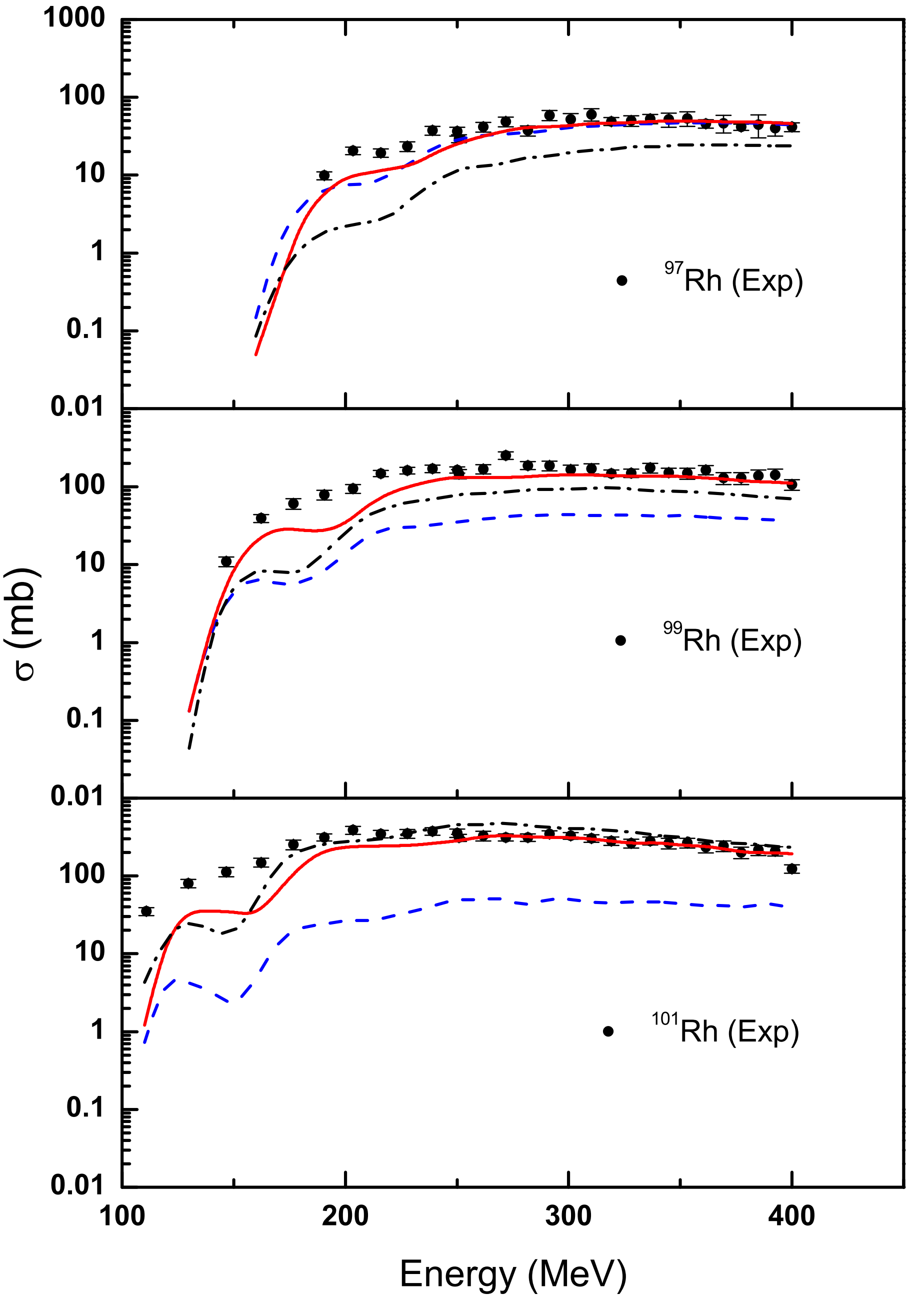

Figure 2.6: Excitation function of Rh residues formed in the interaction of ^{14}N with ^{103}Rh as indicated. Also see the caption for Fig.2.3 for more details.

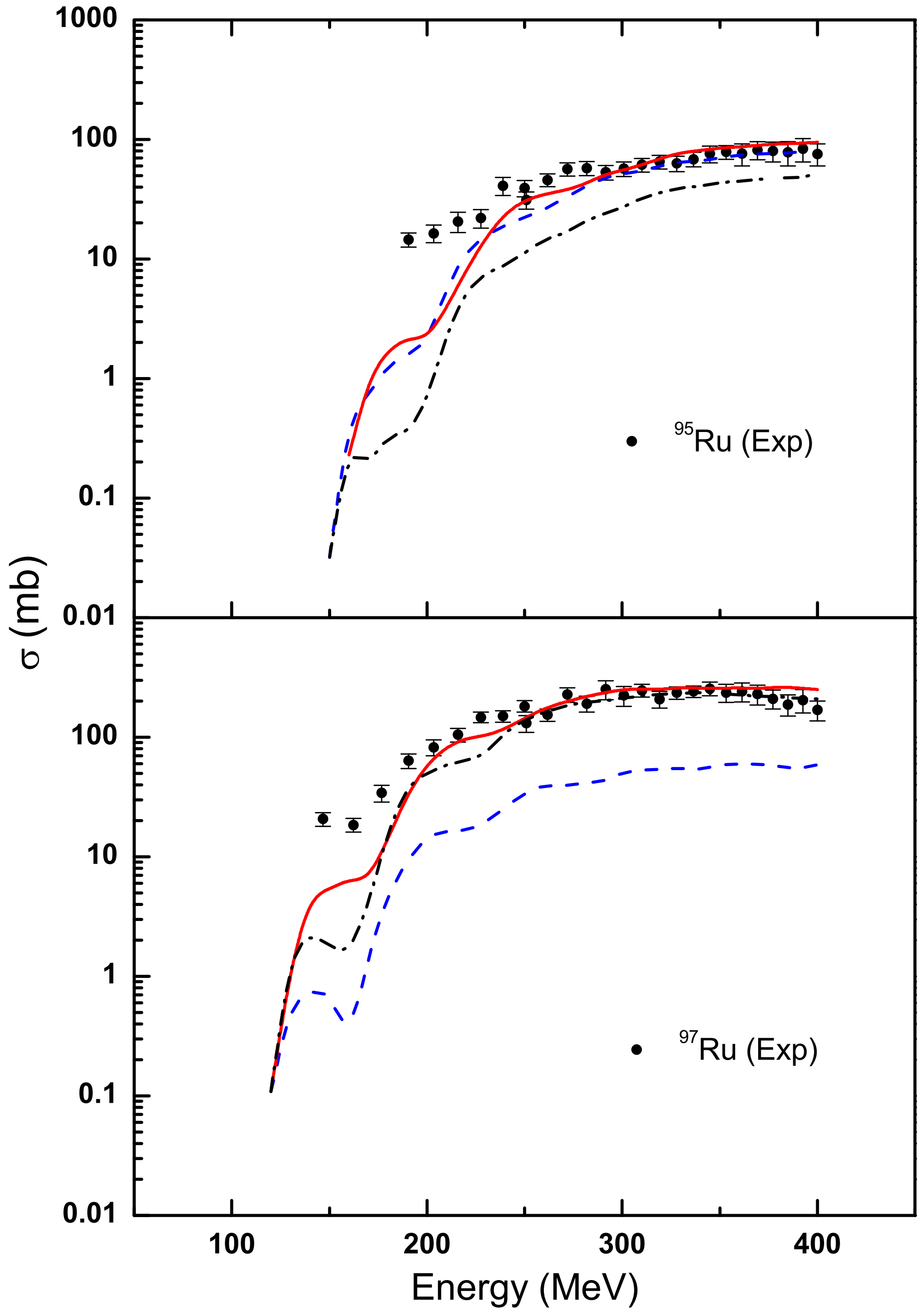

Figure 2.7: Excitation function of Ru residues formed in the interaction of ^{14}N with ^{103}Rh as indicated. Also see the caption for Fig.2.3 for more details.

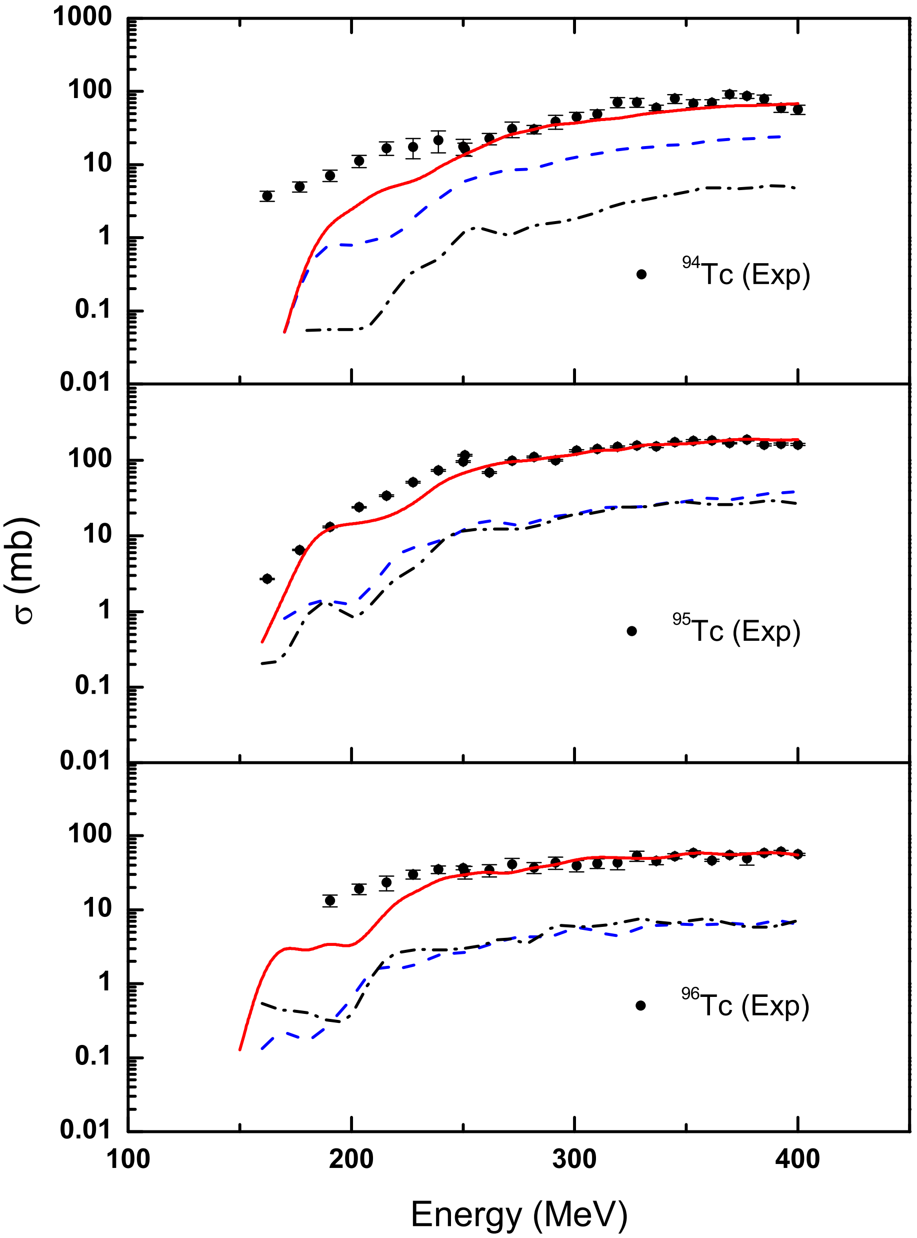

Figure 2.8: Excitation function of Tc residues formed in the interaction of ^{14}N with ^{103}Rh as indicated. Also see the caption for Fig.2.3 for more details.

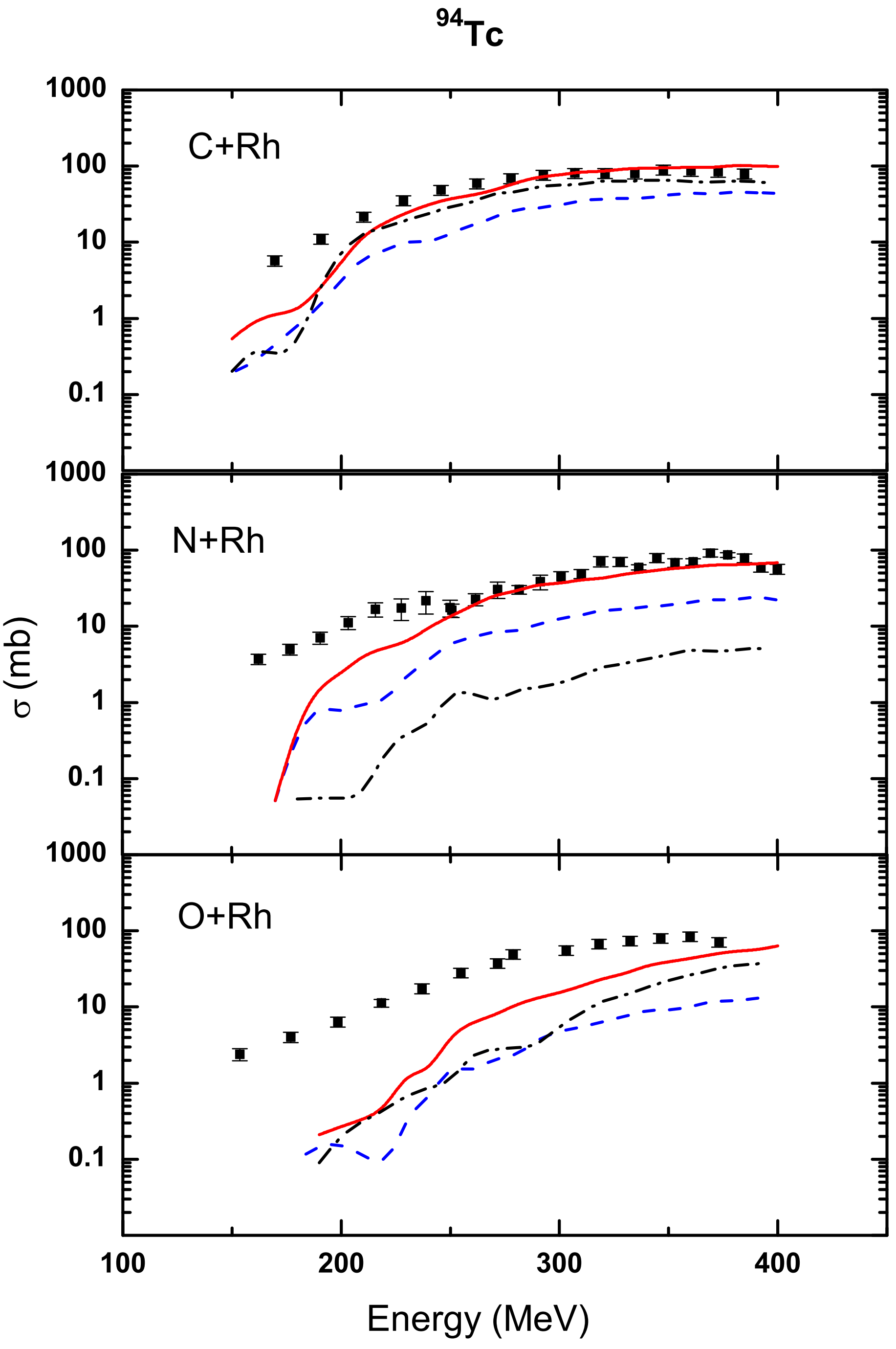

Figure 2.9: Intercomparison of excitation functions of ^{94}Tc for ^{12}C, ^{14}N, and $^{16}O+^{103}Rh$ systems. Theoretical calculations with the HMS model are shown by the solid red curves (OB), the dashed blue curves (FG), and the black dashed-dotted curves (KR).

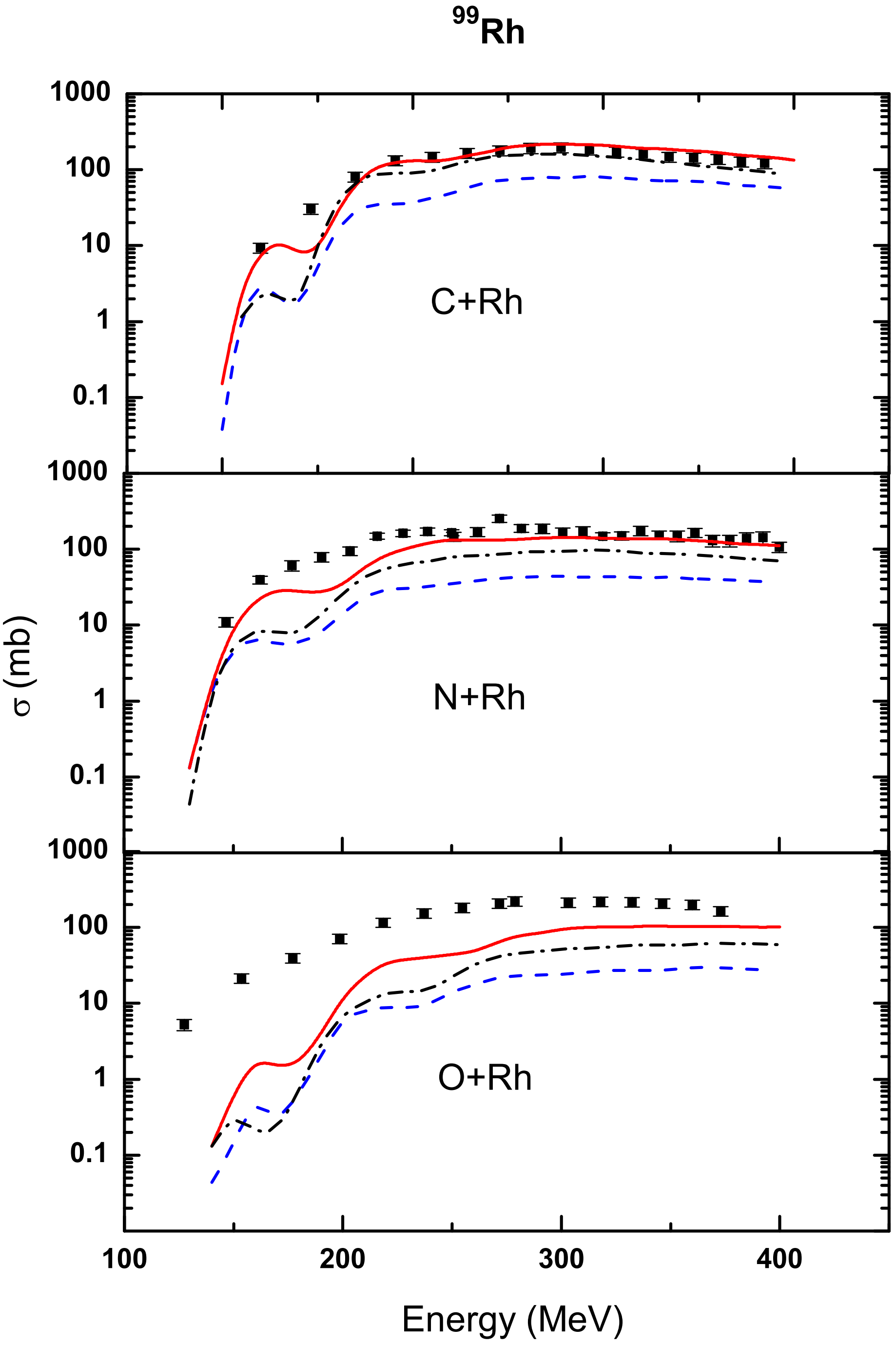

Figure 2.10: Intercomparison of excitation functions of ^{99}Rh for ^{12}C, ^{14}N, and ^{16}O+^{103}Rh systems. Theoretical calculations with the HMS model are shown by the solid red curves (OB), the dashed blue curves (FG), and the black dashed-dotted curves (KR).

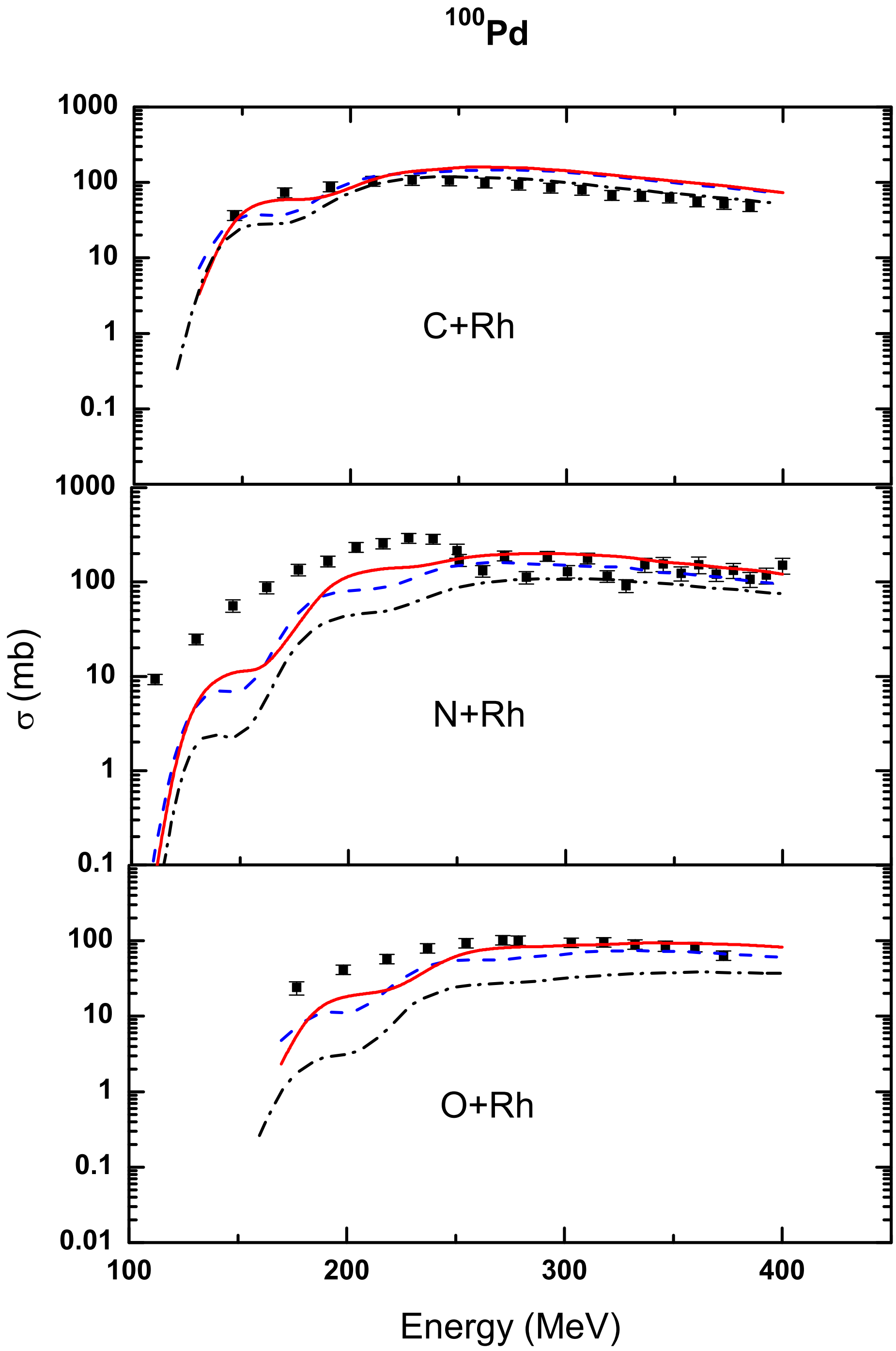

Figure 2.11: Intercomparison of excitation functions of ^{100}Pd for ^{12}C, ^{14}N, and ^{16}O+^{103}Rh systems. Theoretical calculations with the HMS model are shown by the solid red curves (OB), the dashed blue curves (FG), and the black dashed-dotted curves (KR).

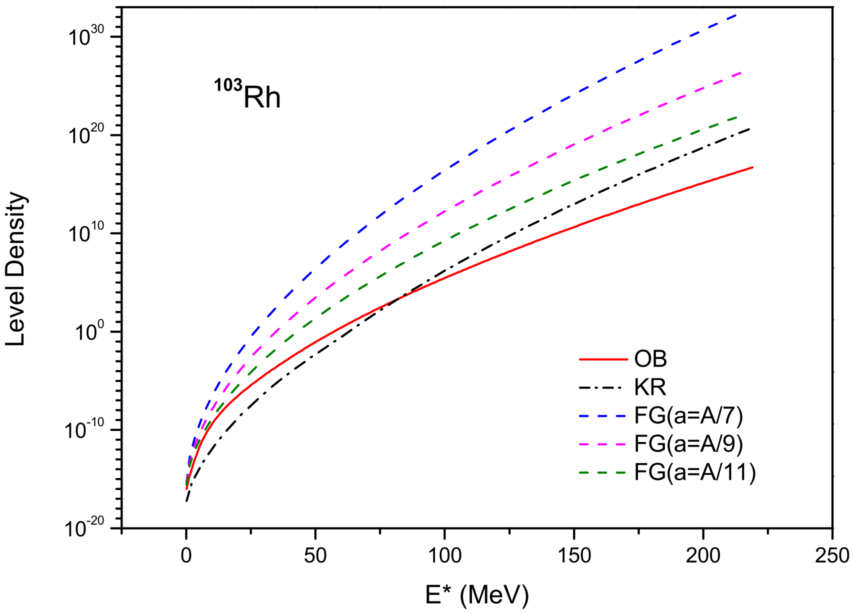

Figure 2.12: Level density of the ^{103}Rh isotope as a function of excitation energy for $l = 0$ for different options as indicated.

✠ ✠ ✠ ✠

Bibliography

[1] M. Cavinato, E. Fabrici, E. Gadioli, E. Gadioli Erba, P. Vergani, M. Crippa, G. Colombo, I. Redaelli, and M. Ripamonti, Phys. Rev. C **52**, 2577 (1995).

[2] E.Z. Buthelezi, F. Cerutti, E. Gadioli, G.F. Steyn, S.H. Connell, and A.A. Cowley, Nucl. Phys. A **753**, 29 (2005).

[3] E.Z. Buthelezi, F. Cerutti, E. Gadioli, G.F. Steyn, A. Pepe, S.H. Connell, and A.A. Cowley, Eur. Phys. J. A **28**, 193 (2006).

[4] M.B. Chadwick, P.G. Young, S. Chiba, S.C. Frankle, G.M. Hale, H.G. Hughes, A.J. Koning, R.C. Little, R.E. MacFarlane, R.E. Prael, and L.S. Waters, Nucl. Sci. Eng. **131**, 293 (1999).

[5] P. Vergani, E. Gadioli, E. Vaciago, E. Fabrici, E. Gadioli Erba, M. Galmarini, G. Ciavola, and C. Marchetta, Phys. Rev. C **48**, 1815 (1993).

[6] E. Gadioli, C. Birattari, M. Cavinato, E. Fabrici, E. Gadioli Erba, V. Allori, F. Cerutti, A. Di Filippo, S. Vailati, T.G. Stevens, S.H. Connell, J.P.F. Sellschop, F.M. Nortier, G.F. Steyn, and C. Marchetta, Nucl. Phys. A **641**, 271 (1998).

[7] E. Gadioli, M. Cavinato, E. Fabrici, E. Gadioli Erba, C. Birattari, I. Mica, S. Solia, G.F. Steyn, S.V. Förtsch, J.J. Lawrie, F.M. Nortier, T.G. Stevens, S.H. Connell, J.P.F. Sellschop, and A.A. Cowley, Nucl. Phys. A **654**, 523 (1999).

[8] C. Birattari, M. Bonardi, M. Cavinato, E. Fabrici, E. Gadioli, E. Gadioli Erba, F. Groppi, M. Bello, C. Bovati, A. Di Filippo, T.G. Stevens, S.H. Connell, J.P.F. Sellschop, S.J. Mills, F.M. Nortier, G.F. Steyn, and C. Marchetta, Phys. Rev. C **54**, 3051 (1996).

[9] M. Blann, Nucl. Phys. A **235**, 211 (1974).

[10] M. Blann and H.K. Vonach, Phys. Rev. C **28**, 1475 (1983).

[11] M. Blann, Annu. Rev. Nucl. Sci. **25**, 123 (1975).

[12] M. Blann and M.B. Chadwick, Phys. Rev. C **57**, 233 (1998).

[13] M.B. Chadwick and P. Obložinský, Phys. Rev. C **50**, 2490 (1994).

[14] E. Gadioli, E. Gadioli Erba, and P.G. Sona, Nucl. Phys. A **217**, 589 (1973).

[15] M. Blann, Phys. Rev. Lett. **28**, 757 (1972).

[16] M. Blann and A.Y. Konobeev, Precompound Cluster Decay in HM-SALICE (2008) (unpublished), available in documentation supplied with RSICC code package PSR-550, https://rsicc.ornl.gov/

[17] M. Blann, Phys. Rev. C **54**, 1341 (1996).

[18] S. G. Mashnik, K. K. Gudima, A. J. Sierk, M. I. Baznat, and N.V. Mokhov, CEM03.01 User Manual, LANL Report No. LA-UR-05-7321, 2005 (unpublished).

[19] J. Blachot, Nucl. Data Sheets **64**, 1 (1991).

[20] D. De Frenne, E. Jacobs, Nucl. Data Sheets **68**, 935 (1993).

[21] J. Blachot, Nucl. Data Sheets **68**, 311 (1993).

[22] J. Blachot, Nucl. Data Sheets **83**, 1 (1998).

[23] B. Singh, Nucl. Data Sheets **81**, 1 (1997).

[24] L.K. Peker, Nucl. Data Sheets **73**, 1 (1994).

[25] A. Artna-Cohen, Nucl. Data Sheets **70**, 85 (1993).

[26] J.K. Tuli, Nucl. Data Sheets **66**, 1 (1992).

[27] L.K. Peker, Nucl. Data Sheets **68**, 165 (1993).

[28] V.F. Weisskopf and D.H. Ewing, Phys. Rev. C **57**, 472 (1940).

[29] S.K. Kataria, V.S. Ramamurthy and S.S. Kapoor, Phys. Rev. C **18**, 549 (1978).

[30] A.V. Ignatyuk, J.L. Weil, S. Raman and S. Kahane, Phys. Rev. C **47**, 1504 (1993).